A theoretical model of reversible adhesion in shape memory surface relief structures and its application in transfer printing

Yeguang Xue [a,b], Yihui Zhang [a,c,*], Xue Feng [c], Seok Kim [d], John A. Rogers [e], Yonggang Huang [a,**]

[a] Department of Engineering Mechanics, Zhejiang University, Hangzhou 310027, China
[b] Departments of Civil and Environmental Engineering and Mechanical Engineering, Center for Engineering and Health, Skin Disease Research Center, Northwestern University, Evanston, IL 60208, USA
[c] Center for Mechanics and Materials, Tsinghua University, Beijing 100084, China
[d] Department of Mechanical Science and Engineering, University of Illinois at Urbana-Champaign, Urbana, IL 61801, USA
[e] Department of Materials Science and Engineering, Frederick Seitz Materials Research Laboratory, University of Illinois at Urbana-Champaign, Urbana, IL 61801, USA

ARTICLE INFO

ABSTRACT

Transfer printing is an important and versatile tool for deterministic assembly and integration of micro/nanomaterials on unusual substrates, with promising applications in fabrication of stretchable and flexible electronics. The shape memory polymers (SMP) with triangular surface relief structures are introduced to achieve large, reversible adhesion, thereby with potential applications in temperature-controlled transfer printing. An analytic model is established, and it identifies two mechanisms to increase the adhesion: (1) transition of contact mode from the triangular to trapezoidal configurations, and (2) explicit enhancement in the contact area. The surface relief structures are optimized to achieve reversible adhesion and transfer printing. The theoretical model and results presented can be exploited as design guidelines for future applications of SMP in reversible adhesion and stretchable electronics.

© 2015 Elsevier Ltd. All rights reserved.

1. Introduction

Transfer printing, as an emerging technique for assembly and integration of two and three dimensional structures of heterogeneous materials at micro/nanoscale, has many important applications in the classes of stretchable/flexible electronic and optoelectronic systems that combine rigid inorganic and deformable organic materials (Meitl et al., 2006; Yoon et al., 2008; Fan et al., 2009; Jeong et al., 2009; Murphy et al., 2009; Park et al., 2009; Carbone et al., 2011; Fakhr et al., 2011; Fang et al., 2011; Guillon et al., 2012; Huang et al., 2012; Xu et al., 2013b; Zhang et al., 2013; Fan et al., 2014; Zhang et al., 2014). Examples of stretchable/flexible systems with functionalities not addressable using previously established technologies include "epidermal" health/wellness monitors (Yu et al., 2012; Kaltenbrunner et al., 2013; Schwartz et al., 2013; Xu et al., 2014), eyeball-like digital cameras (Ko et al., 2008; Song et al., 2013), and sensitive robotic skins (Someya et al., 2004;

Wagner et al., 2004; Mannsfeld et al., 2010; Lu et al., 2012). Transfer printing typically involves the use of a soft elastomeric stamp to transfer solid micro/nanostructured materials (i.e., "inks") from the (donor) substrate where they are generated or grown onto a different (receiver) substrate for device integration (Meitl et al., 2006; Feng et al., 2007; Kim et al., 2010; Carlson et al., 2012a). Several types of transfer printing technologies have been proposed: (1) kinetically controlled transfer printing (Meitl et al., 2006; Feng et al., 2007; Park et al., 2009; Packard et al., 2010; Qi et al., 2011): the viscoelastic stamp is adopted to pick up the micro-devices rapidly and then to print them slowly onto the receiver substrate, enabled by the high and low adhesion strengths at the large and small peeling rates, respectively; (2) surface-relief-assisted transfer printing (Kim et al., 2010; Wu et al., 2011b): surface relief structures (e.g., microtips) are fabricated at the stamp surface to render large surface contact with the inks (and therefore large adhesion force) during pick-up, and small contact area during printing; (3) load-enhanced transfer printing (Kim et al., 2009; Carlson et al., 2011, 2012b): the mechanical loading pro-tocols, such as the directional shearing at the interface and the pressure actuation of a thin elastomeric membrane through microfluidic channels, are employed to enable large and small adhesion forces during pick-up and printing, respectively; (4) laser-driven transfer printing (Li et al., 2012; Saeidpourazar et al., 2012): a laser pulse is adopted during printing to induce large thermal mismatch between the stamp and micro-devices, and therefore initiate separation at the adhesive surface. The key enabling technology of transfer printing is the active control over the interfacial adhesion between the stamp and micro-devices.

Shape memory polymer (SMP) is a type of smart material that can memorize temporary shapes and revert to its permanent shape upon exposure to an external stimulus such as heat (Liu et al., 2007; Yu et al., 2014), light (Koerner et al., 2004; Lendlein et al., 2005), or moisture (Huang et al., 2005a). Several representative mechanics models (Nguyen et al., 2008, 2010; Qi et al., 2008; Long et al., 2009; Ge et al., 2012; Yu et al., 2012; Long et al., 2013) have been established to analyze the underlying mechanisms and stress–strain curves associated with the shape memory effect. When combined with surface relief structures of various patterns (e.g., microprism array, microlens, transmission gratings, which can be fabricated using the technique of compression molding) (Xu et al., 2013a), the shape memory effect can be employed to manipulate the micro-optical performances via temperature change. However, the use of SMP in tuning the interfacial adhesion has been rarely explored. Recently, Eisenhaure et al. (2013) demonstrated experimentally that reversible dry adhesion can be achieved by exploiting the shape memory effect and surface microstructuring, but no theoretical analysis has been reported and the underlying physics is still far from clear. In this paper, a theoretical model is developed for the interfacial adhesion between the microstructured stamp in a general trapezoidal shape and a flat micro-device. The analytic solution of design optimization is obtained for the surface relief structure to maximize the difference of adhesion before and after temperature actuation. Furthermore, the application of this concept in temperature controlled transfer printing is illustrated, which could facilitate automatic operation and selective printing.

2. Design of shape memory surface relief microstructures for reversible adhesion and transfer printing

Fig. 1 illustrates the surface relief structures made of a temperature stimulated SMP that is capable of memorizing one temporary shape, corresponding to dual-shape memory effect (Liu et al., 2007; Xie, 2010). Generally, the shape memory effect can be realized through the glass transition, melting transition, strain induced crystallization transition, etc. In this study, we will focus on the category of SMP realized through melting transition, since melting transition usually gives a sharper recovery event than glass transition (Liu et al., 2007; Ratna and Karger-Kocsis, 2008). For this type of material, there exists a transition temperature T_m (i.e., the melting point) above which the SMP restores its permanent shape. At high temperature ($> T_m$) the permanent configuration of SMP can be deformed into a prescribed configuration by external loads. After cooling down to room temperature ($< T_m$) this deformed configuration can be maintained even when the loads are
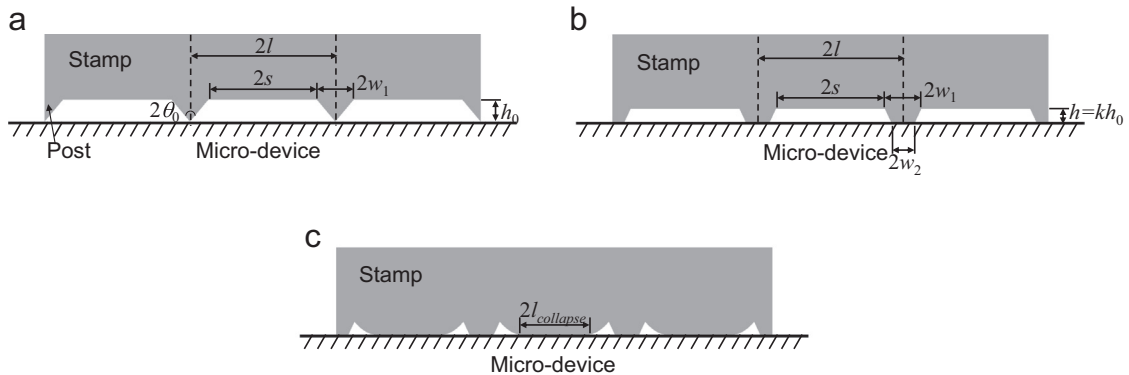

Fig. 1. Schematics of the microstructured stamp in contact with the flat surface of the micro-device. (a) The permanent configuration of the stamp with triangular posts in the absence of roof collapse; (b) the temporary configuration of the stamp with trapezoidal posts in the absence of roof collapse; and (c) the temporary configuration of the stamp with trapezoidal posts in the mode of roof collapse.

removed afterwards. Such configuration is stable at room temperature, and is also called the temporary configuration because it restores to the permanent configuration when it is heated above T_m. For the SMP realized through melting transition, the temporary shape is fixed by crystallization, and the permanent shape is established by chemical or physical cross-linking (Liu et al., 2007). Recently, multi-shape memory effect (Xie, 2010; Yu et al., 2012; Luo et al., 2013) has been achieved that enables phase transitions at multiple levels of temperatures, with the advances in the understanding of the microscopic mechanisms.

The isosceles triangles are designed as the permanent configuration of the surface relief structure in the present study, and they can be fabricated using the technique of compression molding (Xu et al., 2013a). The triangles have a height of h_0 and a top angle of $2\theta_0$, as shown in Fig. 1a, and the length of base is $2w_1 = 2h_0 \tan \theta_0$. The spacing of triangles is $2s$ such that the distance between the centers of adjacent triangles is $2l = 2s + 2w_1$. Under compression along the vertical direction, the triangular surface relief structures (referred to simply as triangular posts in the following) deform approximately into the isosceles trapezoid shown in Fig. 1b, and such temporary configuration can be retained when cooled down from a high temperature ($> T_m$) to room temperature ($< T_m$). The lengths of the parallel sides of the trapezoidal posts are $2w_1$ (top) and $2w_2$ (bottom), and the reduced height is $h = kh_0$, with k (< 1) denoting the compression ratio. For the incompressible SMP (Xu et al., 2013a), i.e., with the Poisson's ratio $\nu \approx 0.5$, the geometric parameters of the triangle and trapezoid satisfy $h_0 w_1/2 = kh_0(w_1 + w_2)/2$ in a plane strain model, which gives $w_2 = (1 - k)w_1/k$. The present study is limited to $w_2 \leq w_1$, i.e., $k \geq 1/2$. As the reduced post height (i.e., $h = kh_0$) of the temporary trapezoidal configuration decreases, the state of roof collapse shown in Fig. 1c may be triggered, mainly due to the adhesion between stamp and micro-device, which will be analyzed in detail in Section 3.

By switching the configuration of the surface relief structures between triangles and trapezoids, the contact area (and therefore the adhesion energy) between the surface relief structure and micro-device can be varied to a large extent through optimization of post geometry. Such reversible adhesion has important applications in temperature-controlled transfer printing, as schematically illustrated in Fig. 2, which has the advantage of selective printing over the conventional transfer printing techniques. Fig. 2a–c describe the pick-up process of micro-device from the donor substrate by using the SMP
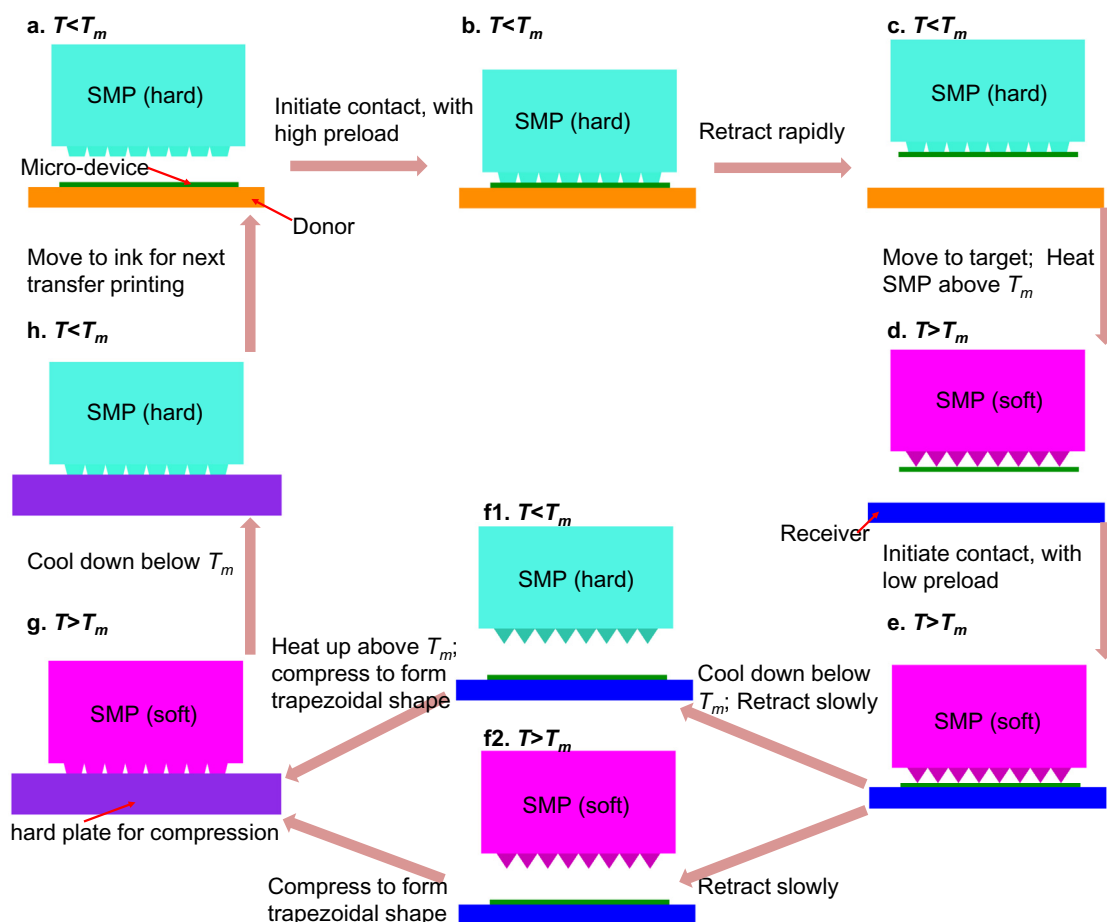

Fig. 2. Schematic illustration for applications of microstructured SMP in transfer printing. The permanent configuration of the surface relief structures has low adhesion with the micro-device, while the temporary configuration, compressed from the triangular posts, in contrast, has much larger adhesion to bond with the micro-device. In this schematic, the difference of adhesion arises solely from explicit shape change of posts without roof collapse.

stamp with trapezoidal posts that correspond to the temporary configuration. Heated above the transition temperature T_m, the posts recover to the permanent configuration in the triangular shape, which is then used to complete the printing of micro-device onto the receiver substrate, as shown in Fig. 2d–f. Since the SMP usually has varied modulus at different temperatures, the two different cases of printing process are taken into account, including the room-temperature ($< T_m$) and high-temperature ($> T_m$) printing, corresponding to Fig. 2f1 and f2, respectively. After finishing the printing of micro-device, the SMP stamp needs to be compressed and cooled down to form the temporary trapezoidal configuration again for cyclic uses, as shown from Fig. 2g–a. From this operation process, it is clear that the geometry of the surface relief structures can be optimized to achieve a large difference of adhesion between the triangular and trapezoidal configurations, which will be analyzed, in a quantitative manner, in the following sections.

3. A theoretical model of reversible adhesion and contact mode

Fig. 1 shows that two types of mechanisms, explicit enhancement of contact area (from Fig. 1a and b), and transition of contact mode (from Fig. 1a–c), could lead to adhesion change between trapezoidal and triangular posts. The contact mode between the posts and micro-device is mainly determined by the competition between adhesion energy and deformation energy due to roof collapse. For periodically distributed rectangular posts, Huang et al. (2005b) developed an analytic model to derive mathematically the requirement to occur roof collapse and the contact length due to roof collapse. This model is extended for trapezoidal posts in the following. From the energetic point of view, roof collapse only occurs if the total potential energy U_{total} for the collapsed state (in Fig. 1c) is less than its counterpart, zero, for the un-collapsed state (in Fig. 1b). Here U_{total} can be expressed as

$$U_{total} = U_{deformation} - 2l_{collapse}\gamma, \tag{1}$$

where $U_{deformation}$ is the deformation energy for the collapsed configuration, and the second term corresponds to the adhesion energy, with γ representing the work of adhesion between the stamp and micro-device, and $2l_{collapse}$ the collapse length (Fig. 1c) to be determined. As shown in the Appendix A, the deformation energy is given by

$$U_{deformation} = \frac{\bar{E}_{eff} h^2}{4} \frac{K\left(l_{collapse}/(l - w_2)\right)}{K\left[\sqrt{1 - (l_{collapse}^2/(l - w_2)^2)}\right]}, \tag{2}$$

where $h = kh_0$ (Fig. 1b) is the reduced post height, $K(x) = \int_0^{\pi/2} (1 - x^2 \sin^2\varphi)^{-1/2} d\varphi$ is the complete elliptic integral of first kind, and

$$\bar{E}_{eff} = \frac{E}{1 - \nu^2} \frac{\pi^2 (1 - (w_2/l))^2}{4 \ln (\csc(\pi w_2/2l))} \approx E \frac{\pi^2 (1 - (w_2/l))^2}{3 \ln (\csc(\pi w_2/2l))} \tag{3}$$

is the effective plane-strain Young's modulus (see Appendix A for details). Here E and $\nu \approx 0.5$ are the Young's modulus and Poisson's ratio of the SMP, respectively. Substitution of Eq. (2) into Eq. (1) gives

$$U_{total} = \frac{\bar{E}_{eff} h^2}{4} \left\{ \frac{K\left(l_{collapse}/(l - w_2)\right)}{K\left[\sqrt{1 - l_{collapse}^2/(l - w_2)^2}\right]} - \frac{8(l - w_2)\gamma}{\bar{E}_{eff} h^2} \frac{l_{collapse}}{l - w_2} \right\}. \tag{4}$$

Its minimization, $dU_{total}/dl_{collapse} = 0$, gives the collapse length to depend on the normalized work of adhesion $\bar{\gamma} = 8(l - w_2)\gamma / (\bar{E}_{eff} h^2)$, i.e., $l_{collapse}/(l - w_2) = F(\bar{\gamma})$, where the non-dimensional function F is obtained from

$$\frac{d}{dF}\left[\frac{K(F)}{K\left(\sqrt{1 - F^2}\right)} \right] = \bar{\gamma}, \tag{5}$$

and is shown in Fig. 3.[1] The minimal total potential energy, normalized by $\bar{E}_{eff} h^2/4$, is then $[K(F)/K(\sqrt{1 - F^2})] - \bar{\gamma}F$ and depends only on $\bar{\gamma}$. The state of roof collapse is stable only when the minimal total potential energy is less than its counterpart, zero, for the un-collapsed state (in Fig. 1b). This gives the condition for stable collapse as

$$\bar{\gamma} = \frac{8(l - w_2)\gamma}{\bar{E}_{eff} h^2} > 1.40. \tag{6}$$

The contact length $l_{contact}^{trapezoidal} = 2(w_2 + l_{collapse})$, which is important to the optimal design for reversible adhesion and transfer printing in the following two sections, gives the fraction of contact as

---

[1] Eq. (5) holds only when the collapse length is shorter than the spacing ($2s$) of the posts.
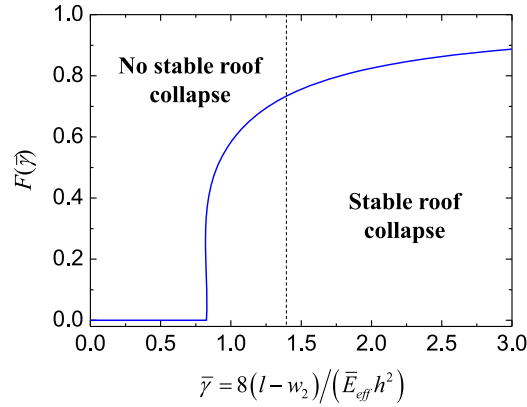
Fig. 3. Function F versus the normalized work of adhesion $\bar{\gamma} = 8(l - w_2)\gamma \big/ \big(\bar{E}_{eff} h^2\big)$.

$$\bar{l}_{contact}^{trapezoidal} = \frac{l_{contact}^{trapezoidal}}{2l} = \frac{w_2}{l} + \left(1 - \frac{w_2}{l}\right)F(\bar{\gamma}) \ \text{ for } \ \bar{\gamma} > 1.40. \tag{7a}$$

This equation indicates that the fraction of contact depends only on two non-dimensional parameters, i.e., w_2/l and $\bar{\gamma}$, or equivalently, w_2/l and $\gamma l/(Eh^2)$ since it can be rewritten as

$$\bar{l}_{contact}^{trapezoidal} = \frac{w_2}{l} + \left(1 - \frac{w_2}{l}\right)F\left[\frac{\gamma l}{Eh^2}\frac{24\ln\left(\csc\left(\pi w_2/2l\right)\right)}{\pi^2(1 - w_2/l)}\right]H\left[\frac{\gamma l}{Eh^2}\frac{24\ln\left(\csc\left(\pi w_2/2l\right)\right)}{\pi^2(1 - w_2/l)} - 1.40\right], \tag{7b}$$

where H is the Heaviside step function[2] such that the above equation also holds for the case of no stable collapse. Fig. 4 shows the fraction of contact versus $\gamma l/(Eh^2)$ for different values of w_2/l. It remains a constant w_2/l for $\gamma l/(Eh^2)$ less than a critical value to trigger stable roof collapse, and increases sharply at the critical value.

Then we analyze another important aspect of the reversible adhesion, i.e., whether the trapezoidal post at high temperature ($> T_m$) is able to peel away from the micro-device to restore to the triangular shape, considering the softening of SMP due to melting transition. Here, the shape recovery of posts is decided mainly by the competition of the elastic energy stored in the trapezoidal posts as compressed from the triangular shape, and the adhesion energy due to the contact with the micro-device. The adhesion energy is determined by the contact length, i.e.,

$$U_{adhesion}^{post} = \gamma w_2 = \gamma w_1 \frac{1 - k}{k}, \tag{8}$$

and the elastic energy is proportional to the reduced elastic modulus $E_{reduced}$ at high temperature ($> T_m$) and square of w_1, i.e.
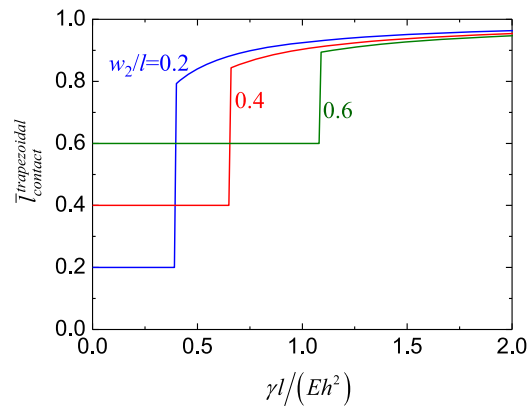

Fig. 4. Scaling laws of the fraction of contact $\bar{l}_{contact}^{trapezoidal}$ versus the normalized parameter, $\gamma l/(Eh^2)$, for three different values of w_2/l.

---

[2] The Heaviside step function $H(x)$ is defined as $H(x) = \begin{cases} 0, & x \leq 0 \\ 1, & x > 0 \end{cases}$.

$$U_{deformation}^{post} = E_{reduced} w_1^2 f(\theta, k),\tag{9}$$

where $f(\theta, k)$ is a dimensionless function in terms of the angle θ and compression ratio k, which can be calculated by finite element simulations. A successful shape recovery requires the stored elastic energy to be larger than the adhesion energy, or equivalently:

$$\frac{U_{deformation}^{post}}{U_{adhesion}^{post}} = \frac{E_{reduced} w_1}{\gamma} f(\theta, k) > 1.\tag{10}$$

For a typical SMP obtained by crosslinking semi-crystalline poly(ethylene-co-vinyl acetate) (EVA), the work of adhesion is $\gamma = 0.04$ J/m² (Bistac et al., 1998), and the reduced modulus is $E_{reduced} \approx 1.0$ MPa (Li et al., 2011) at a temperature (~ 80 °C) higher than the melting point ($T_m \sim 66$ °C). The ratio $U_{deformation}^{post}/U_{adhesion}^{post}$ can be obtained with the aid of finite element simulations, as shown in Fig. 5 for a representative base length $w_1 = 20$ μm (and therefore, $E_{reduced} w_1/\gamma = 500$). It increases monotonously with the decrease of compression ratio (k) and top angle (2θ). For a compression ratio smaller than ~ 0.94, $U_{deformation}^{post}/U_{adhesion}^{post}$ is much larger than 1 for all three representative top angles (60°, 90° and 120°), indicating that the post can restore successfully to the permanent (triangular) configuration when heated to ~ 80 °C. For other combinations of material and post dimension that give $E_{reduced} w_1/\gamma > 500$, the ratio $U_{deformation}^{post}/U_{adhesion}^{post}$ would be even larger, and the shape recovery will be easier to complete. In this study, appropriate post geometries and SMP materials will adopted to yield a ratio of $U_{deformation}^{post}/U_{adhesion}^{post}$ that is much larger than 1, to ensure successful shape recovery.

4. Design optimization of microstructured SMP for reversible adhesion

To facilitate the reversible adhesion between stamp and micro-device, it is important to have a large change of adhesion due to the shape memory effect. The key to achieve remarkable change of adhesion energy between the permanent (triangular) and temporary (trapezoidal) configurations in Section 3 is to maximize their difference in the contact area. This is equivalent to

1) maximization of $\bar{l}_{contact}^{trapezoidal}$ in Eq. (7b) for trapezoidal posts; and
2) minimization of the fraction of contact for the triangular posts, which is ensured if the triangular posts do not collapse, i.e.,

$$\frac{\gamma l}{E h_0^2} \frac{24 \ln(\csc(\pi R_{contact}/2l))}{\pi^2 (1 - (R_{contact}/l))} < 1.40\tag{11a}$$

following the same approach as in Eq. (6), where $R_{contact} = 32(1 - \nu^2)\gamma \tan^2\theta_0/(\pi E) \approx 24\gamma \tan^2\theta_0/(\pi E)$ is the contact radius of an ideally sharp triangular post with a flat micro-device due to adhesion (Wu et al., 2011a), which should be less than the bottom length of the trapezoidal posts (w_2) such that $k < \left\{1 + \left[24\gamma w_1/\left(\pi E h_0^2\right)\right]\right\}^{-1}$. Eq. (11a) is rewritten as

$$\frac{l^2}{w_1^2} \frac{2 \ln\left(\csc(12\gamma w_1^2/E h_0^2 l)\right)}{\pi^2 E h_0^2 l/12\gamma w_1^2 - 2\pi} < 1.40 \text{ for } \frac{1}{2} \leq k < \frac{1}{1 + 24\gamma w_1/\pi E h_0^2}.\tag{11b}$$

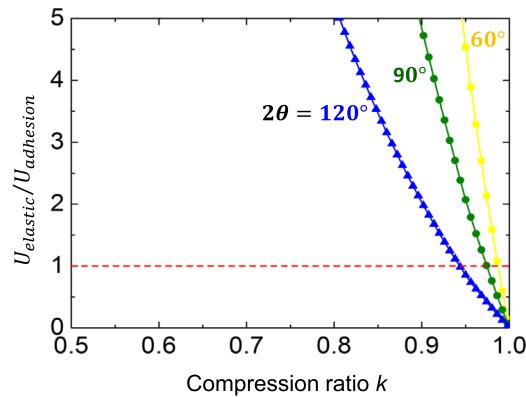The corresponding fraction of contact is

Fig. 5. Ratio of stored elastic energy in the trapezoidal posts as compressed from the triangular shape to the adhesion energy as a function of compression ratio (k) for three different top angles (60°, 90° and 120°). The dashed line corresponds to the critical state when the stored elastic energy equals to the adhesion energy.

$$\bar{l}_{contact}^{triangular} = \frac{R_{contact}}{l} = \frac{24\gamma w_1^2}{\pi E h_0^2 l} = \pi k^2 \frac{1 - (w_2/l)}{\ln\left(\csc(\pi w_2/2l)\right)} \frac{w_1^2}{l^2} \bar{\gamma}. \tag{12}$$

For each compression ratio k (between $1/2$ and 1), w_1 and h_0 are optimized in order to maximize:

$$\bar{l}_{contact}^{trapezoidal} - \bar{l}_{contact}^{triangular} =$$

$$
\begin{cases}
\dfrac{w_2}{l} + \left(1 - \dfrac{w_2}{l}\right)F(\bar{\gamma}) - \pi k^2 \dfrac{1 - (w_2/l)}{\ln\left(\csc(\pi w_2/2l)\right)} \dfrac{w_1^2}{l^2} \bar{\gamma} & for \quad \dfrac{l^2}{w_1^2} \dfrac{2\ln\left(\csc(12\gamma w_1^2/Eh_0^2 l)\right)}{\pi^2 Eh_0^2 l/12\gamma w_1^2 - 2\pi} < 1.40 < \bar{\gamma} \\[1.5em]
\dfrac{w_2}{l} - \pi k^2 \dfrac{1 - (w_2/l)}{\ln\left(\csc(\pi w_2/2l)\right)} \dfrac{w_1^2}{l^2} \bar{\gamma} & for \quad \bar{\gamma} < 1.40
\end{cases}
\tag{13}
$$

under the constraint $k < \{1 + [24\gamma w_1/(\pi E h_0^2)]\}^{-1}$. It can be rewritten, via Eqs. (3) and (6) and $w_2 = (1 - k)w_1/k$, in terms of three non-dimensional parameters w_2/l, k and $\bar{\gamma}$ as

$$\bar{l}_{contact}^{trapezoidal} - \bar{l}_{contact}^{triangular} = \frac{w_2}{l} - \frac{\pi k^4}{(1-k)^2} \frac{(1 - (w_2/l))(w_2^2/l^2)}{\ln\left(\csc(\pi w_2/2l)\right)} \bar{\gamma} + \left(1 - \frac{w_2}{l}\right)F(\bar{\gamma})H(\bar{\gamma} - 1.40) \tag{14}$$

for

$$\bar{\gamma} < \frac{(1-k)^2}{\pi k^4} \frac{\ln\left(\csc(\pi w_2/2l)\right)}{(1 - (w_2/l))(w_2^2/l^2)} \min\left(\frac{w_2}{l}, \lambda\right), \tag{15}$$

where λ is obtained from

$$\frac{\lambda \ln\left(\csc(\pi\lambda/2)\right)}{1 - \lambda} = 1.40 \frac{\pi k^2}{(1-k)^2} \frac{w_2^2}{l^2}, \tag{16a}$$

or equivalently:

$$\frac{\lambda \ln\left(\csc(\pi\lambda/2)\right)}{1 - \lambda} = 1.40\pi \frac{w_1^2}{l^2}, \tag{16b}$$

i.e., $\lambda = \lambda(w_1/l)$.[3] For each k, the maximum of Eq. (14) with respect to w_2/l and $\bar{\gamma}$ occurs when $\bar{\gamma} = 0$ or at its upper bound in Eq. (15) (see Appendix B for details), which gives

$$
\left(\bar{l}_{contact}^{trapezoidal} - \bar{l}_{contact}^{triangular}\right)_{max}
$$

$$
= \max \left\langle \begin{array}{l}
\dfrac{(1-k)w_1}{kl}, \\[1em]
\dfrac{(1-k)w_1}{kl} - \min\left[\dfrac{(1-k)w_1}{kl}, \lambda\right] \\[1em]
+ \left[1 - \dfrac{(1-k)w_1}{kl}\right]F\left\{\dfrac{1}{\pi k^2} \dfrac{\ln\left[\csc((\pi(1-k)w_1/2kl))\right]}{[1 - (((1-k)w_1)/kl)]\frac{w_1^2}{l^2}} \min\left[\dfrac{(1-k)w_1}{kl}, \lambda\right]\right\}
\end{array} \right\rangle.
\tag{17}
$$

For $(w_1/l)(1/\lambda) < k/(1-k)$, it is simplified to

$$
\left(\bar{l}_{contact}^{trapezoidal} - \bar{l}_{contact}^{triangular}\right)_{max}
$$

$$
= \max \left\langle \dfrac{(1-k)w_1}{kl}, \left[1 - \dfrac{(1-k)w_1}{kl}\right]F\left\{\dfrac{1-k}{\pi k^3} \dfrac{\ln\left[\csc((\pi(1-k)w_1)/2kl))\right]}{[1 - ((1-k)w_1)/kl]w_1/l}\right\} \right\rangle.
\tag{18}
$$

For $(w_1/l)(1/\lambda) > k/(1-k)$, Eq. (17) becomes

---

[3] For $w_1/l > 0.284$, Eq. (16b) has no solution, which corresponds to $\lambda \to +\infty$. For $w_1/l < 0.284$, Eq. (16b) has two solutions, and λ is the smaller one between the two.

$$\left(\bar{l}_{contact}^{trapezoidal} - \bar{l}_{contact}^{triangular}\right)_{max}$$

$$= \max\left\langle \frac{(1-k)w_1}{kl}, \frac{(1-k)w_1}{kl} - \lambda + \left[1 - \frac{(1-k)w_1}{kl}\right]F\left\{\frac{1}{\pi k^2}\frac{\ln\left[\csc(\pi(1-k)w_1)/2kl\right]}{[1-(1-k)w_1/kl]w_1^2/l^2}, \lambda\right\}\right\rangle. \tag{19}$$

Fig. 6 shows the difference in contact area in Eq. (17) [or equivalently Eqs. (18) and (19)] versus the normalized base length w_1/l for several compression ratios k between 0.5 and 1. For each k, the straight segment on the right corresponds to optimized, un-collapsed state, whereas the curvilinear part on the left corresponds to the optimized, collapsed state. The dot on each curve clearly shows the maximum difference in contact area achieved for each compression ratio k.

Figs. 7a and b give the maximum difference in contact area and the corresponding normalized base length w_1/l obtained from Fig. 6 versus the compression ratio k, respectively. The normalized adhesion energy $\gamma l/(Eh_0^2)$ corresponding to the maximum difference in contact area is also given in Fig. 7b. The vertical line in each figure clearly shows the collapsed and un-collapsed states to its right and left, respectively. Fig. 7b gives the optimized design [of normalized base length w_1/l and adhesion energy $\gamma l/(Eh_0^2)$] for each compression ratio.

5. The microstructured SMP for transfer printing

The analytic model in Sections 3 and 4 for the microstructured SMP is extended for temperature-controlled transfer printing (Fig. 2) in this section. The trapezoidal configuration is used during the pick-up process of micro-devices since large adhesion is required. Specifically, the adhesive force at the stamp/device interface, $\gamma_{stamp}l_{contact}^{trapezoidal}$, should be larger than that at the device/donor interface, $\gamma_{donor}l$, where $\gamma_{stamp} = \gamma$ and γ_{donor} denote the work of adhesion at the stamp/device and donor/device interfaces, respectively. This gives

$$\bar{l}_{contact}^{trapezoidal} > \frac{\gamma_{donor}}{\gamma}, \tag{20}$$

where $\bar{l}_{contact}^{trapezoidal} = \bar{l}_{contact}^{trapezoidal}\left[w_2/l, \gamma l/(Eh^2)\right] = \bar{l}_{contact}^{trapezoidal}\left[(1-k)w_1/(kl), \gamma l/\left(k^2Eh_0^2\right)\right]$ is obtained from Eq. (7b) and is shown in Fig. 4. On the other hand, small adhesion is needed to facilitate printing of micro-devices onto the desired receiver substrate. The triangular post recovered from the shape memory effect is therefore ideal for this purpose. This requires a lower adhesive force at the stamp/device interface, $\gamma_{stamp}l_{contact}^{triangular}$, than that at the receiver/device interface, $\gamma_{receiver}l$, i.e.,

$$\bar{l}_{contact}^{triangular} < \frac{\gamma_{receiver}}{\gamma}, \tag{21}$$

where $\gamma_{receiver}$ denotes the work of adhesion between the receiver material and the micro-device, and

$$\bar{l}_{contact}^{triangular} = \frac{24\gamma w_1^2}{\pi Eh_0^2 l} + \left(1 - \frac{24\gamma w_1^2}{\pi Eh_0^2 l}\right)F\left[\frac{\gamma l}{Eh_0^2}\frac{24\ln\left(\csc(12\gamma w_1^2/Eh_0^2 l)\right)}{\pi^2\left(1-(24\gamma w_1^2/\pi Eh_0^2 l)\right)}\right]H\left[\frac{\gamma l}{Eh_0^2}\frac{24\ln\left(\csc(12\gamma w_1^2/Eh_0^2 l)\right)}{\pi^2\left(1-(24\gamma w_1^2/\pi Eh_0^2 l)\right)} - 1.40\right] \tag{22}$$

is obtained from Eq. (7b) by replacing w_2 and h with $R_{contact}$ and h_0, respectively. The above equation degenerates to Eq. (12) for no collapse of the triangular post. For a highly adhesive receiver $\gamma_{receiver} \geq \gamma$, Eq. (21) always holds since $\bar{l}_{contact}^{triangular} < 1 \leq \gamma_{receiver}/\gamma$. Eqs. (20) and (21) provide the bounds for $\gamma l/(Eh_0^2)$ and w_1/l.

In the following examples the widely adopted silicon device is adopted, and the stamp is made of an elastomeric SMP
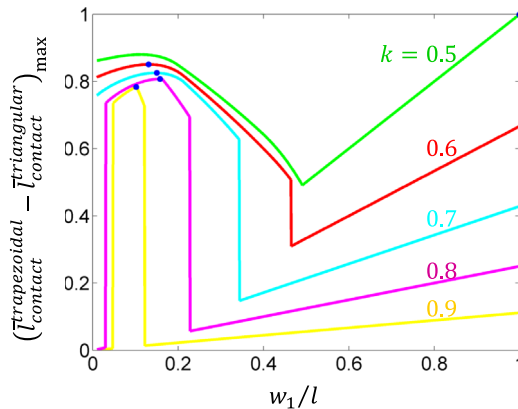

Fig. 6. Maximum difference in contact area after optimization with regard to λ, shown as a function of the normalized base length w_1/l for different compression ratios k. The blue circular points denote the maximum of each curve.
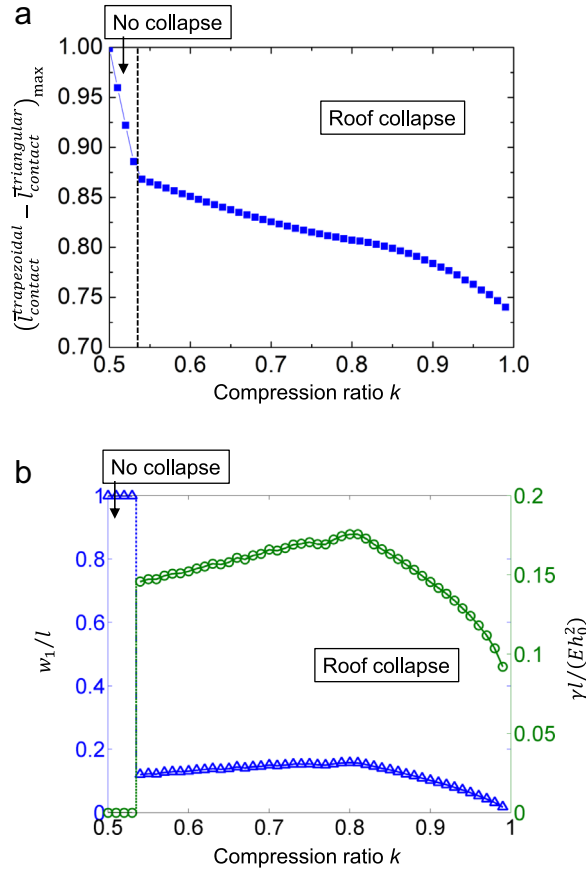
Fig. 7. Design optimization of permanent configuration to achieve largest difference in contact area. (a) $\left(\bar{l}_{contact}^{trapezoidal} - \bar{l}_{contact}^{triangular}\right)_{max}$ for different compression ratios, and (b) the corresponding geometric parameters [w_1/l and $\gamma l/\left(Eh_0^2\right)$] of the triangular post.

obtained by crosslinking semi-crystalline poly(ethylene-co-vinyl acetate) (EVA) which is a low-cost commodity polymer widely used in industry (Li et al., 2011). The EVA has the work of adhesion, $\gamma_{stamp}=0.04$ J/m^2 (Bistac et al., 1998), Young's modulus $E_{room}=14.3$ MPa at room temperature (Li et al., 2011), and the reduced modulus $E_{reduced} \approx 1.0$ MPa at a temperature (~ 80 °C) higher than the melting point ($T_m \sim 66$ °C).[4] In comparison to the stamp, the work of adhesion between silicon device and donor (e.g., silicon wafer) is usually much lower, e.g., $\gamma_{donor}=0.006$ J/m^2 (Tsukruk and Bliznyuk, 1998). A wide range of receiver materials with the work of adhesion $\gamma_{receiver}$ ranging from 0.004 J/m^2 to 0.4 J/m^2, corresponding to 1/10 to 10 times of the work of adhesion of PDMS (Kim et al., 2010), is considered. In the first set of analyses, the permanent configuration (triangles) of the posts is considered to be already cooled down to room temperature, before the micro-devices are printed, as shown in Fig. 2f1. Therefore, $E_{room}=14.3$ MPa is used for both the trapezoidal and triangular posts. Fig. 8a–c shows the regions of postdesign for successful transfer printing in the space of w_1/l and $\gamma l/\left(Eh_0^2\right)$ for the work of adhesion $\gamma_{receiver}=0.004$ J/m^2 and the compression ratio $k=0.5$, 0.6 and 0.7. The region of post design gradually reduces with the increase of compression ratio (k), and even splits into two separate regions for $k=0.7$ (Fig. 8c), with the left and right parts representing "roof collapse" and "no roof collapse" in the trapezoidal posts, respectively. For a highly adhesive receiver (e.g., $\gamma_{receiver} \geq 0.04$ J/m^2), the area of valid region (in Fig. 8d–f) enlarges tremendously.

In practical applications, the printing of micro-devices can be also operated when the SMP stamp is just recovered to the permanent configuration and is still maintained at high temperature ($T > T_m$), as shown in Fig. 2f2. In comparison to the room-temperature printing, the high-temperature printing does not require the process of cooling down the triangular posts (in Fig. 2e) and heating it up again after printing, thereby reducing the time of transfer printing process. In this analyses, $E_{room}=14.3$ MPa and $E_{reduced}=1.0$ MPa are adopted for trapezoidal and triangular posts, respectively. The corresponding regions of design for successful transfer printing, shown in Fig. 9a–c for $k=0.5$, 0.6 and 0.7, are reduced as compared to Fig. 8a–c for room-temperature printing. No collapse would occur in the trapezoidal post for successful transfer printing because of the small $\gamma l/\left(E_{room}h_0^2\right)$ for successful printing. For a relative large compression ratio (e.g., $k=0.7$), the valid

---

[4] 66 °C corresponds to the temperature at the initial stage of melting transition in the EVA, and the modulus will reduce rapidly to reach a plateau (~ 1.0 MPa) after the completion of melting transition. To ensure the stable operation of transfer printing process, 80 °C is adopted for the high-temperature printing in the analyses, since the modulus is not sensitive to temperature change at this stage.
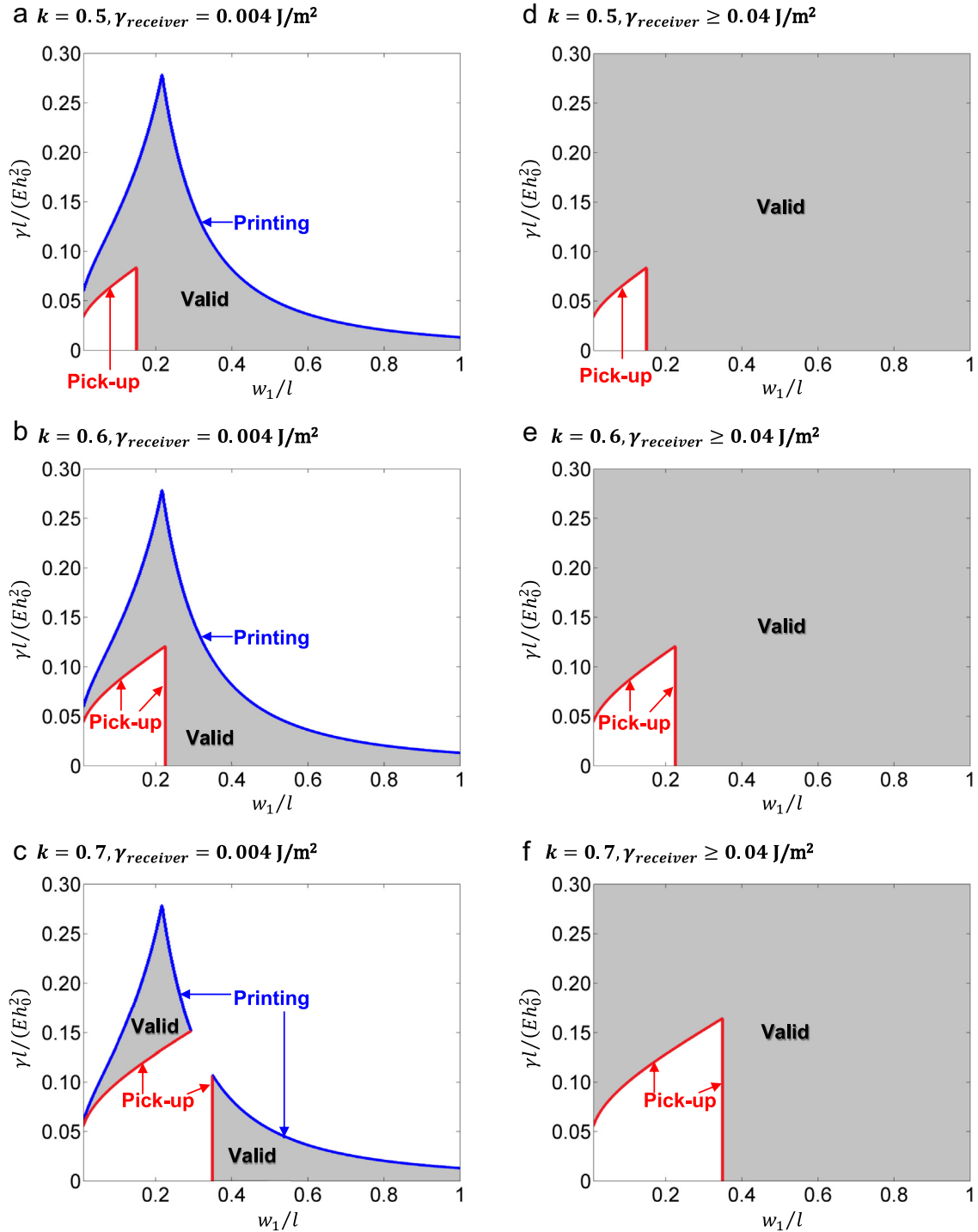
Fig. 8. Valid post designs in terms of w_1/l and $\gamma l/\left(Eh_0^2\right)$ to achieve successful transfer printing with the pick-up and printing both operated at room temperature. (a), (b) and (c) correspond to the valid design regions for $\gamma_{receiver}=0.004$ J/m² and the compression ratio of $k=0.5$, 0.6, and 0.7, respectively. (d), (e) and (f) correspond to the valid design regions for $\gamma_{receiver} \geq 0.04$ J/m² and the compression ratio of $k=0.5$, 0.6, and 0.7, respectively. The labels 'pick-up' and 'printing' correspond to the boundaries of valid design regions, representing the critical states for successful picking-up and printing.

region becomes quite narrow, indicating that very limited combinations of w_1/l and $\gamma l/\left(E_{room}h_0^2\right)$ can be used. Therefore, an appropriate spacing of posts and a relative large compression are required to form the temporary configuration when the SMP triangular posts are adopted to print the micro-devices at high temperature.
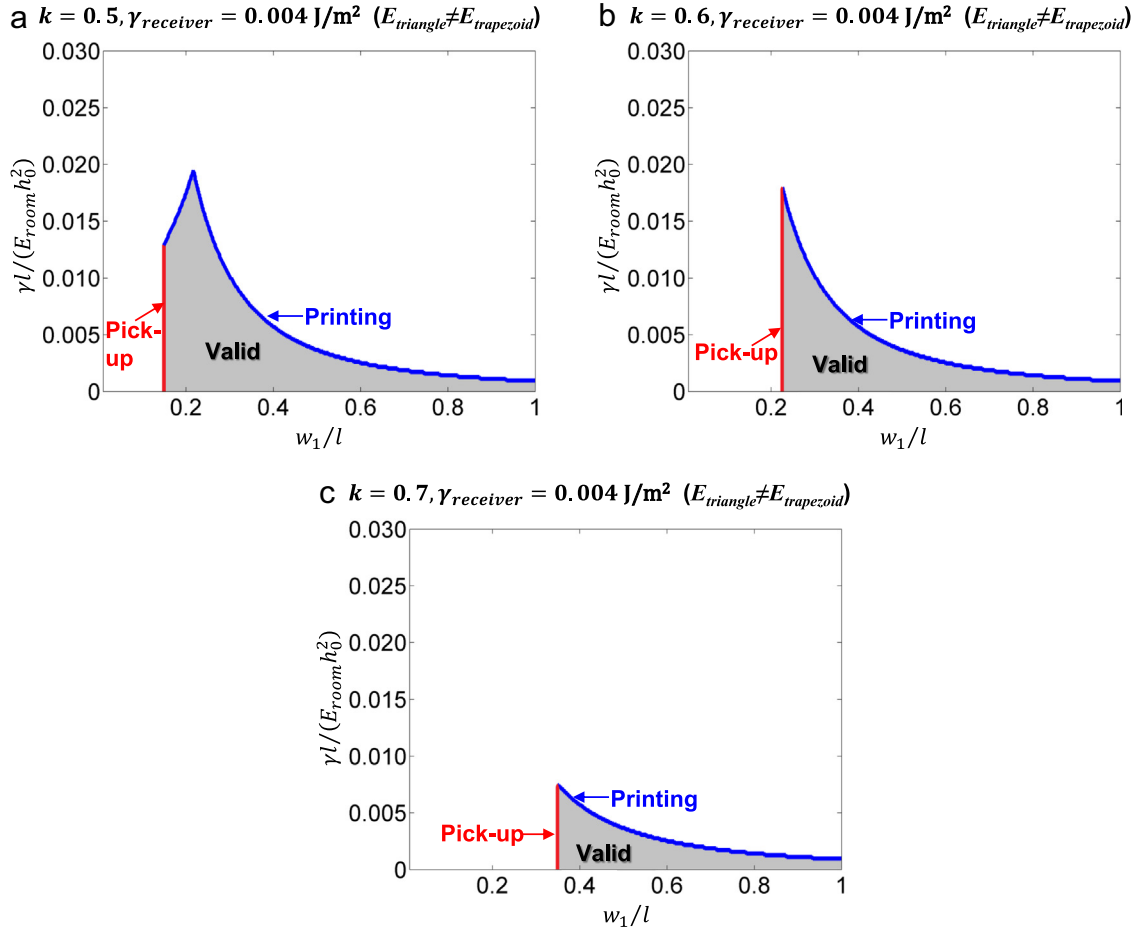
Fig. 9. Valid post designs in terms of w_1/l and $\gamma l/\left(E_{room}h_0^2\right)$ to achieve successful transfer printing with room-temperature pick-up and high-temperature printing. (a), (b) and (c) correspond to the valid design regions for $\gamma_{receiver}=0.004$ J/m^2 and the compression ratio of $k=0.5$, 0.6, and 0.7, respectively. The labels 'pick-up' and 'printing' correspond to the boundaries of valid design regions, representing the critical states for successful picking-up and printing.

6. Viscoelastic effect of SMP on the design diagram of transfer printing

The above analyses mainly apply for the case that the time scale involved in the process of heating and cooling is sufficiently long to ensure the equilibrium states are reached, i.e., the permanent and temporary configurations are fully recovered and fixed as designed. Practically, the viscoelastic effect may come into play, especially for the softened SMP at high temperature. This section gives an approximate estimation of viscoelastic effect of SMP on the design diagram of transfer printing, by analyzing the time-dependent recovery process of SMP post after heated above transition temperature (T_m).

Several representative constitutive models of thermally induced SMP have been developed in the framework of finite deformation theory (Nguyen et al., 2008; Qi et al., 2008; Ge et al., 2012), which could capture well the viscoelastic/plastic effects. To simplify the analyses and provide some approximate estimations, a simple standard linear solid model (Gutierrez-Lemini, 2014), as widely used for viscoelastic materials, is adopted in the following analyses. This model offers the simplest option to describe the shape memory effect for the SMP containing two phases (i.e., fixed phase and reversible phase), which could provide good predictions of measured recover ratio during reheating (Lin and Chen, 1999). As shown in Fig. 10a, this model adopts a linear combination of springs and dashpots to represent elastic and viscous components, in which E_r and η_r denote the elastic modulus and viscosity for the reversible phase, and E_f denotes the elastic modulus for the fixed phase. Considering a temporary configuration of SMP with uniform strain ε_0, we assume the material is rapidly heated to a high temperature ($> T_m$) and then maintained at this temperature. Under a stress-free condition, the time-dependent recovery ratio, defined as $R(t) = 1 - \varepsilon(t)/\varepsilon_0$, then follows an exponential law as $R(t) = 1 - e^{-E_f t/\eta_r}$, with ε denoting the engineering strain at the current time. By using this equation to estimate the time-dependent height recovery of SMP posts, the viscoelastic effect on the design diagram of transfer printing can be evaluated approximately.
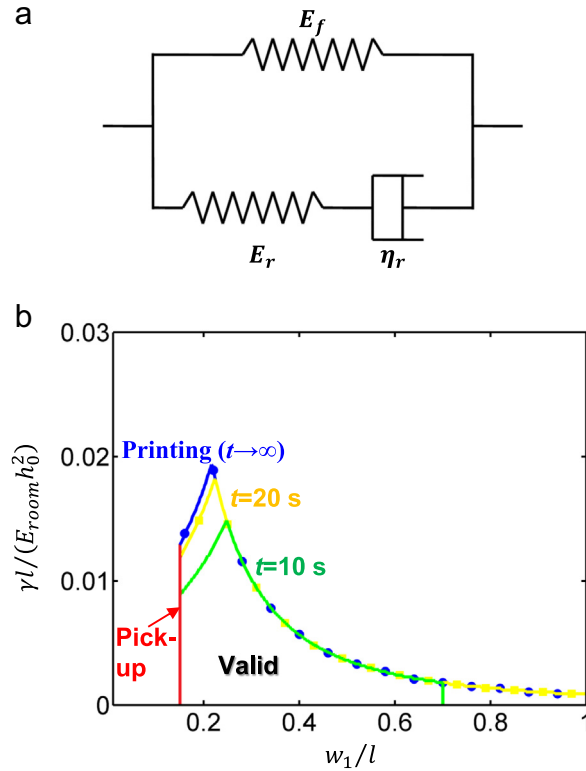
Fig. 10. Schematic illustration (a) of the standard linear solid model and valid post designs (b) in terms of w_1/l and $\gamma l/\left(E_{room} h_0^2\right)$ by accounting for the viscoelastic effect. The valid design regions are calculated using $\gamma_{receiver} = 0.004$ J/m^2 and the compression ratio of $k=0.5$. The labels 'pick-up' and 'printing' correspond to the boundaries of valid design regions, representing the critical states for successful picking-up and printing.

For the EVA material studied in previous sections, the material parameters at ∼80 °C are given by $\eta_r = 1.0$MPa·s and $E_f = 0.14$MPa, which are approximated through numerical fitting of the storage modulus, loss modulus and recovery ratio measured in experiments (Li et al., 1999; Khonakdar et al., 2004; Li et al., 2011). The calculations show the recovery ratio as $R(t = 10s) \approx 0.753$, $R(t = 20s) \approx 0.939$ and $R(t = 30s) \approx 0.985$, indicating the system could reach the equilibrium state after around half a minute. Fig. 10b illustrates that the valid design region approaches the results of equilibrium-state theory with increasing the time for shape recovery. But the area of valid region narrows obviously if a rapid printing (e.g., ∼10 s after heating up) is targeted.

7. Concluding remarks and discussions

An analytic model of adhesion and contact mode for the surface relief structure of SMP in a general trapezoidal configuration is established. The analytic solution for the optimized surface relief structure is obtained for reversible adhesion between the permanent triangular posts and the temporary trapezoidal posts formed by compression. Two mechanisms are identified for the increase of adhesion in the trapezoidal posts, which are further explored in the applications of temperature-controlled transfer printing. This study provides design guidelines of SMP microstructured surfaces for future applications in reversible adhesion and transfer printing.

Beside the adhesion control through the change of contact area, the SMP microstructured surface could also achieve large difference in the pull-off force between the low-temperature trapezoidal post and high-temperature triangular post, because of the reduced modulus at high temperature (Eisenhaure et al., 2013). This will be considered in our future study.

Acknowledgments

Appendix A. Deformation energy of the trapezoidal post with roof collapse

By considering the collapsed configuration of trapezoidal post as a type of equivalent crack (with a length $2l - 2w_2$) and using the principle of linear superposition, the deformation energy for the case of single crack can be solved following Huang et al. (2005b) as

$$U_{deformation}^{single-crack} = \frac{\bar{E}h^2}{4} \frac{K\left(l_{collapse}/(l - w_2)\right)}{K\left[\sqrt{1 - \left(l_{collapse}^2/(l - w_2)^2\right)}\right]}, \tag{A.1}$$

where the effect of elastic mismatch between the soft stamp and rigid micro-device is taken into account, and $\bar{E} = E/(1 - \nu^2) = 4E/3$ is the plane-strain modulus. To further account for the periodic distribution of trapezoidal posts and the effect of adjacent posts, Huang et al. (2005b) showed that the ratio of deformation energy ($U_{deformation}^{periodic-cracks}$) for periodic cracks to that ($U_{deformation}^{single-crack}$) for a single crack is approximately given by

$$\frac{U_{deformation}^{periodic-cracks}}{U_{deformation}^{single-crack}} = \frac{\pi^2(1 - (w_2/l))^2}{4\ln(\csc(\pi w_2/2l))}. \tag{A.2}$$

Therefore, the deformation energy can be approximated by Eq. (2), with $\bar{E}_{eff}$ given by Eq. (3).

Appendix B. Optimization of $\bar{l}_{contact}^{trapezoidal} - \bar{l}_{contact}^{triangular}$

For a given compression ratio k, $\bar{l}_{contact}^{trapezoidal} - \bar{l}_{contact}^{triangular}$ in Eq. (13) is maximized with respect to w_1/l and $\bar{\gamma}$ under the constraints in Eq. (11). This is done separately for $\bar{\gamma} < 1.4$ and $\bar{\gamma} > 1.4$ in the following:

1) For $\bar{\gamma} < 1.40$, $\bar{l}_{contact}^{trapezoidal} - \bar{l}_{contact}^{triangular}$ decreases as $\bar{\gamma}$ increases; therefore, $\bar{l}_{contact}^{trapezoidal} - \bar{l}_{contact}^{triangular}$ achieves the maximum w_2/l at $\bar{\gamma} = 0$.
2) For $1.40 < \bar{\gamma} < ((1 - k)^2/\pi k^4)(\ln(\csc(\pi w_2/2L))/(1 - (w_2/l))w_2^2/l^2 \min(w_2/l, \lambda)$, the local maximum (if it exists) is determined by the vanishing derivative of Eq. (13), $d\left(\bar{l}_{contact}^{trapezoidal} - \bar{l}_{contact}^{triangular}\right)/d\bar{\gamma} = 0$, or equivalently

$$\frac{dF(\bar{\gamma})}{d\bar{\gamma}} = \frac{1}{(d^2/dF^2)\left[(K(F(\bar{\gamma})))/K\left(\sqrt{1 - F(\bar{\gamma})^2}\right)\right]} = \frac{\pi k^2}{\ln(\csc(\pi w_2/2l))} \frac{w_1^2}{l^2}. \tag{B.1}$$

The local maximum is then compared to the values at the two ends of $\bar{\gamma}$ in order to determine the maximum $\bar{l}_{contact}^{trapezoidal} - \bar{l}_{contact}^{triangular}$ with respect to $\bar{\gamma}$. This is further maximized with respect to w_1/l. The numerical results suggest that, for each k, maximization of $\bar{l}_{contact}^{trapezoidal} - \bar{l}_{contact}^{triangular}$ with respect to w_1/l corresponds only to $\bar{\gamma} = 0$ or $\bar{\gamma} = \left(((1 - k)^2)/\pi k^4\right)(\ln(\csc(\pi w_2/2l)))/(1 - (w_2/l))(w_2^2/l^2)\min(w_2/l, \lambda)$, as shown in Fig. B1, which then leads to Eq. (17).
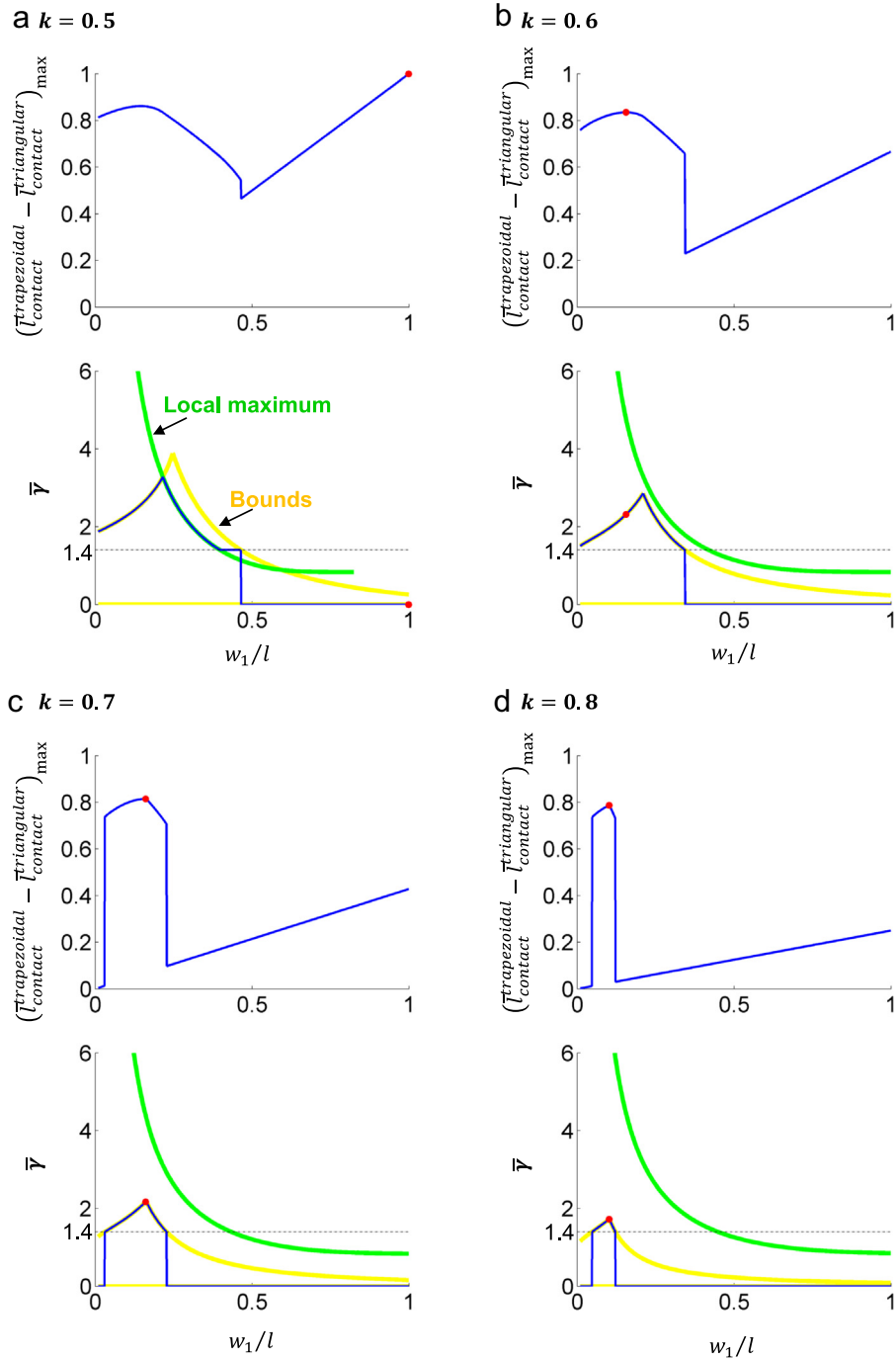
Fig. B1. Maximum difference in contact area, $(\bar{l}_{contact}^{trapezoidal} - \bar{l}_{contact}^{triangular})_{max}$, after optimization with regard to $\bar{\gamma}$, shown as a function of the normalized base length w_1/l and the corresponding $\bar{\gamma}$ (in blue color) for different compression ratios of $k=0.5$ (a), 0.6 (b), 0.7 (c) and 0.8 (d). The red circular points denote the maximum $(\bar{l}_{contact}^{trapezoidal} - \bar{l}_{contact}^{triangular})_{max}$ for different w_1/l. The green and yellow curves represent the local maximum and bounds for $\bar{\gamma}$, respectively.

References

Bistac, S., Kunemann, P., Schultz, J., 1998. Tentative correlation between contact angle hysteresis and adhesive performance. J. Colloid Interface Sci. 201, 247–249.

Carbone, G., Pierro, E., Gorb, S.N., 2011. Origin of the superior adhesive performance of mushroom-shaped microstructured surfaces. Soft Matter 7, 5545–5552.

Carlson, A., Kim-Lee, H.J., Wu, J., Elvikis, P., Cheng, H.Y., Kovalsky, A., Elgan, S., Yu, Q.M., Ferreira, P.M., Huang, Y.G., Turner, K.T., Rogers, J.A., 2011. Shear-enhanced adhesiveless transfer printing for use in deterministic materials assembly. Appl. Phys. Lett. 98, 264104.

Carlson, A., Bowen, A.M., Huang, Y.G., Nuzzo, R.G., Rogers, J.A., 2012a. Transfer printing techniques for materials assembly and micro/nanodevice fabrication. Adv. Mater. 24, 5284–5318.

Carlson, A., Wang, S.D., Elvikis, P., Ferreira, P.M., Huang, Y.G., Rogers, J.A., 2012b. Active, programmable elastomeric surfaces with tunable adhesion for deterministic assembly by transfer printing. Adv. Funct. Mater. 22, 4476–4484.

Eisenhaure, J.D., Xie, T., Varghese, S., Kim, S., 2013. Microstructured shape memory polymer surfaces with reversible dry adhesion. ACS Appl. Mater. Interfaces 5, 7714–7717.

Fakhr, O., Altpeter, P., Karrai, K., Lugli, P., 2011. Easy fabrication of electrically insulating nanogaps by transfer printing. Small 7, 2533–2538.

Fan, J.A., Yeo, W.H., Su, Y.W., Hattori, Y., Lee, W., Jung, S.Y., Zhang, Y.H., Liu, Z.J., Cheng, H.Y., Falgout, L., Bajema, M., Coleman, T., Gregoire, D., Larsen, R.J., Huang, Y.G., Rogers, J.A., 2014. Fractal design concepts for stretchable electronics. Nat. Commun. 5, 3266.

Fan, Z.Y., Ho, J.C., Takahashi, T., Yerushalmi, R., Takei, K., Ford, A.C., Chueh, Y.L., Javey, A., 2009. Toward the development of printable nanowire electronics and sensors. Adv. Mater. 21, 3730–3743.

Fang, H., Madsen, M., Carraro, C., Takei, K., Kim, H.S., Plis, E., Chen, S.Y., Krishna, S., Chueh, Y.L., Maboudian, R., Javey, A., 2011. Strain engineering of epitaxially transferred, ultrathin layers of III–V semiconductor on insulator. Appl. Phys. Lett. 98, 012111.

Feng, X., Meitl, M.A., Bowen, A.M., Huang, Y., Nuzzo, R.G., Rogers, J.A., 2007. Competing fracture in kinetically controlled transfer printing. Langmuir 23, 12555–12560.

Ge, Q., Luo, X.F., Rodriguez, E.D., Zhang, X., Mather, P.T., Dunn, M.L., Qi, H.J., 2012. Thermomechanical behavior of shape memory elastomeric composites. J. Mech. Phys. Solids 60, 67–83.

Guillon, S., Salomon, S., Seichepine, F., Dezest, D., Mathieu, F., Bouchier, A., Mazenq, L., Thibault, C., Vieu, C., Leichle, T., Nicu, L., 2012. Biological functionalization of massively parallel arrays of nanocantilevers using microcontact printing. Sens. Actuators B-Chem. 161, 1135–1138.

Gutierrez-Lemini, D., 2014. Engineering Viscoelasticity. Springer-Verlag, New York.

Huang, W.M., Yang, B., An, L., Li, C., Chan, Y.S., 2005a. Water-driven programmable polyurethane shape memory polymer: demonstration and mechanism. Appl. Phys. Lett. 86, 114105.

Huang, Y.A., Wang, X.M., Duan, Y.Q., Bu, N.B., Yin, Z.P., 2012. Controllable self-organization of colloid microarrays based on finite length effects of electrospun ribbons. Soft Matter 8, 8302–8311.

Huang, Y.G.Y., Zhou, W.X., Hsia, K.J., Menard, E., Park, J.U., Rogers, J.A., Alleyne, A.G., 2005b. Stamp collapse in soft lithography. Langmuir 21, 8058–8068.

Jeong, H.E., Lee, J.K., Kim, H.N., Moon, S.H., Suh, K.Y., 2009. A nontransferring dry adhesive with hierarchical polymer nanohairs. Proc. Natl. Acad. Sci. 106, 5639–5644.

Kaltenbrunner, M., Sekitani, T., Reeder, J., Yokota, T., Kuribara, K., Tokuhara, T., Drack, M., Schwodiauer, R., Graz, I., Bauer-Gogonea, S., Bauer, S., Someya, T., 2013. An ultra-lightweight design for imperceptible plastic electronics. Nature 499, 458–463.

Khonakdar, H.A., Wagenknecht, U., Jafari, S.H., Hassler, R., Eslami, H., 2004. Dynamic mechanical properties and morphology of polyethylene/ethylene vinyl acetate copolymer blends. Adv. Polym. Technol. 23, 307–315.

Kim, S., Wu, J.A., Carlson, A., Jin, S.H., Kovalsky, A., Glass, P., Liu, Z.J., Ahmed, N., Elgan, S.L., Chen, W.Q., Ferreira, P.M., Sitti, M., Huang, Y.G., Rogers, J.A., 2010. Microstructured elastomeric surfaces with reversible adhesion and examples of their use in deterministic assembly by transfer printing. Proc. Natl. Acad. Sci. 107, 17095–17100.

Kim, T.H., Carlson, A., Ahn, J.H., Won, S.M., Wang, S.D., Huang, Y.G., Rogers, J.A., 2009. Kinetically controlled, adhesiveless transfer printing using microstructured stamps. Appl. Phys. Lett. 94, 113502.

Ko, H.C., Stoykovich, M.P., Song, J.Z., Malyarchuk, V., Choi, W.M., Yu, C.J., Geddes, J.B., Xiao, J.L., Wang, S.D., Huang, Y.G., Rogers, J.A., 2008. A hemispherical electronic eye camera based on compressible silicon optoelectronics. Nature 454, 748–753.

Koerner, H., Price, G., Pearce, N.A., Alexander, M., Vaia, R.A., 2004. Remotely actuated polymer nanocomposites – stress-recovery of carbon-nanotube-filled thermoplastic elastomers. Nat. Mater. 3, 115–120.

Lendlein, A., Jiang, H.Y., Junger, O., Langer, R., 2005. Light-induced shape-memory polymers. Nature 434, 879–882.

Li, F.K., Zhu, W., Zhang, X., Zhao, C.T., Xu, M., 1999. Shape memory effect of ethylene-vinyl acetate copolymers. J. Appl. Polym. Sci. 71, 1063–1070.

Li, J.J., Rodgers, W.R., Xie, T., 2011. Semi-crystalline two-way shape memory elastomer. Polymer 52, 5320–5325.

Li, R., Li, Y.H., Lu, C.F., Song, J.Z., Saeidpouraza, R., Fang, B., Zhong, Y., Ferreira, P.M., Rogers, J.A., Huang, Y.G., 2012. Thermo-mechanical modeling of laser-driven non-contact transfer printing: two-dimensional analysis. Soft Matter 8, 7122–7127.

Lin, J.R., Chen, L.W., 1999. Shape-memorized crosslinked ester-type polyurethane and its mechanical viscoelastic model. J. Appl. Polym. Sci. 73, 1305–1319.

Liu, C., Qin, H., Mather, P.T., 2007. Review of progress in shape-memory polymers. J. Mater. Chem. 17, 1543–1558.

Long, K.N., Scott, T.F., Qi, H.J., Bowman, C.N., Dunn, M.L., 2009. Photomechanics of light-activated polymers. J. Mech. Phys. Solids 57, 1103–1121.

Long, R., Qi, H.J., Dunn, M.L., 2013. Thermodynamics and mechanics of photochemcially reacting polymers. J. Mech. Phys. Solids 61, 2212–2239.

Lu, N.S., Lu, C., Yang, S.X., Rogers, J., 2012. Highly sensitive skin-mountable strain gauges based entirely on elastomers. Adv. Funct. Mater. 22, 4044–4050.

Luo, Y.W., Guo, Y.L., Gao, X., Li, B.G., Xie, T., 2013. A general approach towards thermoplastic multishape-memory polymers via sequence structure design. Adv. Mater. 25, 743–748.

Mannsfeld, S.C.B., Tee, B.C.K., Stoltenberg, R.M., Chen, C., Barman, S., Muir, B.V.O., Sokolov, A.N., Reese, C., Bao, Z.N., 2010. Highly sensitive flexible pressure sensors with microstructured rubber dielectric layers. Nat. Mater. 9, 859–864.

Meitl, M.A., Zhu, Z.T., Kumar, V., Lee, K.J., Feng, X., Huang, Y.Y., Adesida, I., Nuzzo, R.G., Rogers, J.A., 2006. Transfer printing by kinetic control of adhesion to an elastomeric stamp. Nat. Mater. 5, 33–38.

Murphy, M.P., Aksak, B., Sitti, M., 2009. Gecko-inspired directional and controllable adhesion. Small 5, 170–175.

Nguyen, T.D., Qi, H.J., Castro, F., Long, K.N., 2008. A thermoviscoelastic model for amorphous shape memory polymers: incorporating structural and stress relaxation. J. Mech. Phys. Solids 56, 2792–2814.

Nguyen, T.D., Yakacki, C.M., Brahmbhatt, P.D., Chambers, M.L., 2010. Modeling the relaxation mechanisms of amorphous shape memory polymers. Adv. Mater. 22, 3411–3423.

Packard, C.E., Murarka, A., Lam, E.W., Schmidt, M.A., Bulovic, V., 2010. Contact-printed microelectromechanical systems. Adv. Mater. 22, 1840–1844.

Park, S.I., Xiong, Y.J., Kim, R.H., Elvikis, P., Meitl, M., Kim, D.H., Wu, J., Yoon, J., Yu, C.J., Liu, Z.J., Huang, Y.G., Hwang, K., Ferreira, P., Li, X.L., Choquette, K., Rogers, J.A., 2009. Printed assemblies of inorganic light-emitting diodes for deformable and semitransparent displays. Science 325, 977–981.

Qi, H.J., Nguyen, T.D., Castroa, F., Yakacki, C.M., ShandaSa, R., 2008. Finite deformation thermo-mechanical behavior of thermally induced shape memory polymers. J. Mech. Phys. Solids 56, 1730–1751.

Qi, Y., Kim, J., Nguyen, T.D., Lisko, B., Purohit, P.K., McAlpine, M.C., 2011. Enhanced piezoelectricity and stretchability in energy harvesting devices fabricated from buckled PZT ribbons. Nano Lett. 11, 1331–1336.

Ratna, D., Karger-Kocsis, J., 2008. Recent advances in shape memory polymers and composites: a review. J. Mater. Sci. 43, 254–269.

Saeidpourazar, R., Li, R., Li, Y.H., Sangid, M.D., Lu, C.F., Huang, Y.G., Rogers, J.A., Ferreira, P.M., 2012. Laser-driven micro transfer placement of prefabricated microstructures. J. Microelectromech. Syst. 21, 1049–1058.

Schwartz, G., Tee, B.C.K., Mei, J.G., Appleton, A.L., Kim, D.H., Wang, H.L., Bao, Z.N., 2013. Flexible polymer transistors with high pressure sensitivity for application in electronic skin and health monitoring. Nat. Commun. 4, 1859.

Someya, T., Sekitani, T., Iba, S., Kato, Y., Kawaguchi, H., Sakurai, T., 2004. A large-area, flexible pressure sensor matrix with organic field-effect transistors for artificial skin applications. Proc. Natl. Acad. Sci. 101, 9966–9970.

Song, Y.M., Xie, Y.Z., Malyarchuk, V., Xiao, J.L., Jung, I., Choi, K.J., Liu, Z.J., Park, H., Lu, C.F., Kim, R.H., Li, R., Crozier, K.B., Huang, Y.G., Rogers, J.A., 2013. Digital cameras with designs inspired by the arthropod eye. Nature 497, 95–99.

Tsukruk, V.V., Bliznyuk, V.N., 1998. Adhesive and friction forces between chemically modified silicon and silicon nitride surfaces. Langmuir 14, 446–455.

Wagner, S., Lacour, S.P., Jones, J., Hsu, P.H.I., Sturm, J.C., Li, T., Suo, Z.G., 2004. Electronic skin: architecture and components. Phys. E Low-Dimens. Syst. Nanostruct. 25, 326–334.

Wu, J., Kim, S., Carlson, A., Lu, C.F., Hwang, K.C., Huang, Y.G., Rogers, J.A., 2011a. Contact radius of stamps in reversible adhesion. Theor. Appl. Mech. Lett. 1, 011001.

Wu, J., Kim, S., Chen, W.Q., Carlson, A., Hwang, K.C., Huang, Y.G., Rogers, J.A., 2011b. Mechanics of reversible adhesion. Soft Matter 7, 8657–8662.

Xie, T., 2010. Tunable polymer multi-shape memory effect. Nature 464, 267–270.

Xu, H.X., Yu, C.J., Wang, S.D., Malyarchuk, V., Xie, T., Rogers, J.A., 2013a. Deformable, programmable, and shape-memorizing micro-optics. Adv. Funct. Mater. 23, 3299–3306.

Xu, S., Zhang, Y.H., Cho, J., Lee, J., Huang, X., Jia, L., Fan, J.A., Su, Y.W., Su, J., Zhang, H.G., Cheng, H.Y., Lu, B.W., Yu, C.J., Chuang, C., Kim, T.I., Song, T., Shigeta, K., Kang, S., Dagdeviren, C., Petrov, I., Braun, P.V., Huang, Y., Paik, U., Rogers, J.A., 2013b. Stretchable batteries with self-similar serpentine interconnects and integrated wireless recharging systems. Nat. Commun. 4, 1543.

Xu, S., Zhang, Y.H., Jia, L., Mathewson, K.E., Jang, K.I., Kim, J., Fu, H.R., Huang, X., Chava, P., Wang, R.H., Bhole, S., Wang, L.Z., Na, Y.J., Guan, Y., Flavin, M., Han, Z. S., Huang, Y.G., Rogers, J.A., 2014. Soft microfluidic assemblies of sensors, circuits, and radios for the skin. Science 344, 70–74.

Yoon, J., Baca, A.J., Park, S.I., Elvikis, P., Geddes, J.B., Li, L.F., Kim, R.H., Xiao, J.L., Wang, S.D., Kim, T.H., Motala, M.J., Ahn, B.Y., Duoss, E.B., Lewis, J.A., Nuzzo, R.G., Ferreira, P.M., Huang, Y.G., Rockett, A., Rogers, J.A., 2008. Ultrathin silicon solar microcells for semitransparent, mechanically flexible and micro-concentrator module designs. Nat. Mater. 7, 907–915.

Yu, K., Xie, T., Leng, J.S., Ding, Y.F., Qi, H.J., 2012. Mechanisms of multi-shape memory effects and associated energy release in shape memory polymers. Soft Matter 8, 5687–5695.

Yu, K., Ge, Q., Qi, H.J., 2014. Reduced time as a unified parameter determining fixity and free recovery of shape memory polymers. Nat. Commun. 5, 3066.

Zhang, Y.H., Xu, S., Fu, H.R., Lee, J., Su, J., Hwang, K.C., Rogers, J.A., Huang, Y., 2013. Buckling in serpentine microstructures and applications in elastomer-supported ultra-stretchable electronics with high areal coverage. Soft Matter 9, 8062–8070.

Zhang, Y.H., Wang, S.D., Li, X.T., Fan, J.A., Xu, S., Song, Y.M., Choi, K.J., Yeo, W.H., Lee, W., Nazaar, S.N., Lu, B.W., Yin, L., Hwang, K.C., Rogers, J.A., Huang, Y., 2014. Experimental and theoretical studies of serpentine microstructures bonded to prestrained elastomers for stretchable electronics. Adv. Funct. Mater. 24, 2028–2037.